Structural Engineering and Mechanics, *Vol. 72, No. 5 (2019) 569-583*
DOI: https://doi.org/10.12989/sem.2019.72.5.569

Finite element simulation for steel tubular members strengthened with FRP under compression

Ahmed M. El-Kholy[*1], Sherif A. Mourad[2a],
Ayman A. Shaheen[1b] and Yomna A. Mohamed[1c]

[1]*Department of Civil Engineering, Faculty of Engineering, Fayoum University, Kiman Fares, El-Fayoum, 63541, Egypt*
[2]*Department of Structural Engineering, Faculty of Engineering, Cairo University, Giza, 12613, Egypt*

(Received February 15, 2019, Revised May 29, 2019, Accepted July 17, 2019)

Abstract. Tubular steel sections are widespread all over the world because of their strength and aesthetic appearance. Tubular steel members may exhibit local buckling such as elephant foot or overall buckling under extreme compression load. Recently, external bonding of fiber reinforced polymers (FRP) sheets for strengthening these members has been explored through experimental research. This paper presents three-dimensional nonlinear finite element analysis (FEA) to investigate the structural behavior of strengthening tubular steel members with FRP against local and overall buckling phenomena. Out-of-roundness and out-of-straightness imperfections were introduced to the numerical models to simulate the elephant foot and overall buckling, respectively. The nonlinear analysis preferences such as the integration scheme of the shell elements, the algorithm for solution of nonlinear equations, the loading procedure, the bisection limits for the load increments, and the convergence criteria were set, appropriately enough, to successfully track the sophisticated buckling deformations. The agreement between the results of both the presented FEA and the experimental research was evident. The FEA results demonstrated the power of the presented rigorous FEA in monitoring the plastic strain distribution and the buckling phenomena (initiation and propagation). Consequently, the buckling process was interpreted for each mode (elephant foot and overall) into three sequential stages. Furthermore, the influence of FRP layers on the nonlinear analysis preferences and the results was presented.

Keywords: tubular steel compression member, FRP strengthening, nonlinear FEA, elephant foot buckling, overall buckling, imperfection

1. Introduction

Steel tubular sections are one of the most aesthetic, versatile and efficient forms for structural members. Many of the impressive structures in the world today would not exist without tubular sections. Steel tubular sections have large second moment of inertia which leads to high bending and torsion strength compared with their light weight. However, it is not without limitations. Having thin walls that are sensitive to the imperfections may cause overall buckling or elephant foot buckling which is elastic-plastic local instability near the tube ends in the shape of an outward bulge. The theoretical elastic buckling load is fictitious because of the existence of imperfections and nonlinearities in real structures. Ostapenko and Grimm (1980) reported that initial geometric imperfection in steel tubular columns may exist in different forms such as out-of-roundness, out-of-straightness and dents. Ohga *et al*. (2001) introduced the buckling mode shapes of thin-walled steel compression members as initial imperfections in finite element stability analysis to investigate the nonlinear behavior of these members. Not only do geometric imperfections exist, but also material imperfections often exist in the steel in form of point, line, plan and volume defects (El-kholy *et al*. 2014). Filling the steel tubes with concrete (Dundu 2012) or less weight and more ductile materials such as steel foam (Moradi and Arwade 2014) increases the load capacity and delays both the overall buckling and the local buckling (partial hoop bulges). Strengthening the existing tubular steel columns is the challenge. Fiber-reinforced polymer (FRP) is used nowadays to strengthen steel hollow members instead of attaching bulky and heavy steel plates. FRP composites have several merits such as high strength to weight ratio, resistance to corrosion, flexibility of following curved surfaces, and orientability in a specific direction unlike steel plates. FRP composites are used to strengthen not only tubular members subjected to axial compression but also those subjected to transverse loads (Narmashiri and Mehramiz 2016).

The research efforts for strengthening steel compression members against elephant foot local buckling gained

*Corresponding author, Assistant Professor
E-mail: ahmed.elkholy@fayoum.edu.eg
[a] Professor
E-mail: smourad@eng.cu.edu.eg
[b] Professor
E-mail: aas8@fayoum.edu.eg
[c] M.Sc. Student
E-mail: yam0@fayoum.edu.eg

http://www.techno-press.com/journals/sem&subpage=7
ISSN: 1225-4568 (Print), 1598-6217 (Online)

momentum during the past decade. Batikha *et al*. (2009) presented theoretical study for innovative strengthening of pinned and fixed steel compression cylinders with small strips of FRP composites in the critical location to eliminate the elephant foot buckling. Teng and Hu (2007) strengthened three steel cylinders with glass fiber reinforced polymers (GFRP), and tested a reference tube and the strengthened tubes under axial compression to study the elephant foot buckling behavior. They presented finite element analysis (FEA) using Abaqus software to investigate the structural behavior of the studied tubes. Chen *et al*. (2006) presented theoretical study for attaching light ring stiffeners at the critical height on the cylindrical wall as a simple remedy to increase the elephant foot capacity of the tubular steel silos and tanks. Nishino and Furkawa (2004) strengthened five tubular steel beam-columns with carbon fiber reinforced polymers composites (CFRP) with prescribed length at both ends of the tube, and tested the six tubes (one bare and five strengthened) under cyclic loading. The strengthened cylinders showed higher deformation capacity besides the elimination of elephant foot buckling. Shaat and Fam (2006) tested twenty-seven short hollow square steel columns (3 bare and 24 CFRP-strengthened) under axial compression to demonstrate the local buckling mode, FRP delamination and FRP rupture. Ghaemdoust *et al*. (2016) reported noticeable elephant foot buckling for square hollow short columns, local buckling (outward and inward deformations) for deficient columns, and strength recovery for deficient members strengthened with CFRP through testing and simulating thirteen specimens.

For the efforts in investigating the overall buckling behavior of tubular steel compression members, the following research papers are summarized. Gao *et al*. (2013) tested five tubular steel long columns (slenderness ratio λ = 80) with unmeasured imperfections (out-of-straightness and minor misalignment in loading) under compression. The monitored overall buckling behavior was followed by local buckling and CFRP delamination at the mid-height of the compressive side of the tubes. Bukovska and Karmazinova (2012) investigated experimentally and numerically the overall buckling resistance of eighteen tubular steel columns (six intact steel tubes and twelve filled by concrete) with λ=54. They measured the real geometry of the eighteen tubes using geodetic methods. Avcar (2014) investigated theoretically and numerically (FEA) the overall buckling of pinned and fixed steel columns with circular, square and rectangular cross sections under axial compression. Shaat and Fam (2006) tested one bare and four CFRP-strengthened square steel columns with different measured out-of-straightness values and constant λ=68. They reported overall buckling behavior followed by local buckling at compression face, and monitored the axial strain on the compression and tension faces. Shahraki *et al*. (2018) reported experimentally and numerically noticeable overall buckling for fourteen deficient steel square hollow compression members (λ=70 and 160) strengthened with either CFRP or steel plates, and concluded that CFRP shows better performance (compared with steel plates) in recovering the member strength.

This paper presents rigorous nonlinear FEA for ten tubular steel members (three bare references and seven FRP-strengthened tubes) under axial compression. These ten tubes were tested by the two research papers that will be reviewed in next section. The presented research demonstrates the FEA power in describing the elephant foot buckling and the overall buckling besides introducing interpretations for the experimental observations.

2. Review of the tested tubes used in the modeling

Two experimental studies were employed in this paper to verify the presented FEA. The employed experimental studies were conducted by Teng and Hu (2007), and Gao *et al*. (2013) to investigate the elephant foot and the overall buckling modes, respectively, of tubular steel compression members. The slenderness ratio of the overall buckling specimens was 80 which is approximately 10 times that of the elephant foot specimens (yielding governs the failure of the specimens with small λ). These ratios are consistent with the elastic buckling theory and the code assumptions. Table 1 lists the steel material properties whereas Table 2 summaries the FRP properties, number of layers and orientation for both experimental studies. In both studies, the epoxy resin was used to bond the fibers together and to the steel surface.

In the elephant foot buckling experimental study, Teng and Hu (2007) tested four steel tubes (one intact and three strengthened) with dimensions (height×diameter×thickness) of 450×165×4.2 mm under axial compression. For the three strengthened specimens, GFRP (1, 2 and 3 layers) was wrapped in hoop direction to provide significant confinement against the elephant foot buckling. The overlapping length between the two sheet ends was 150 mm. Teng and Hu (2007) reported that GFRP-strengthened steel tubes expressed great ductile behavior unlike the bare steel tube. GFRP rupture was obvious at outward buckled locations near the ends of the tubes wrapped with one and two layers unlike that wrapped with three layers where inward buckling dominates the tube failure. Another preliminary observation was that the outward buckling is increasingly restrained and the inward buckling deformation is increasingly magnified with adding new GFRP layers.

In the overall buckling experimental study, Gao *et al*. (2013) tested two bare and five strengthened tubes (2400×88.9×4 mm) under compression loading. For the strengthened tubes, CFRP (2, 4, 6 and 8 layers) was bonded in longitudinal direction above a primary GFRP layer to increase the tube stiffness and resist overall buckling. Gao *et al*. (2013) monitored overall buckling failure for the tested specimens followed by local buckling at maximum compression zone and delamination of CFRP. The authors think that the CFRP failure occurs because that the compressive strength of FRP composites is about half of its tensile strength (Vogler and Kyriakides 2001).

Table 1 Steel properties

Experimental study	Young's modulus (GPa)	Yield stress (MPa)	Ultimate stress (MPa)
Elephant foot buckling	201	333.6	370
Overall buckling	210	355	490

Table 2 FRP properties

Experimetal study	FRP type	Thickness (mm)	Young's modulus (GPa)	Ultimate stress (MPa)	Ultimate strain (%)	Direction	Number of layers
Elephant foot buckling	GFRP	0.17	80.1	1825.5	2.28	Hoop	1,2,3
Overall buckling	GFRP	0.353	28	500	2.0	Vertical	1
	CFRP	0.165	230	3000	1.5	Vertical	2,4,6,8

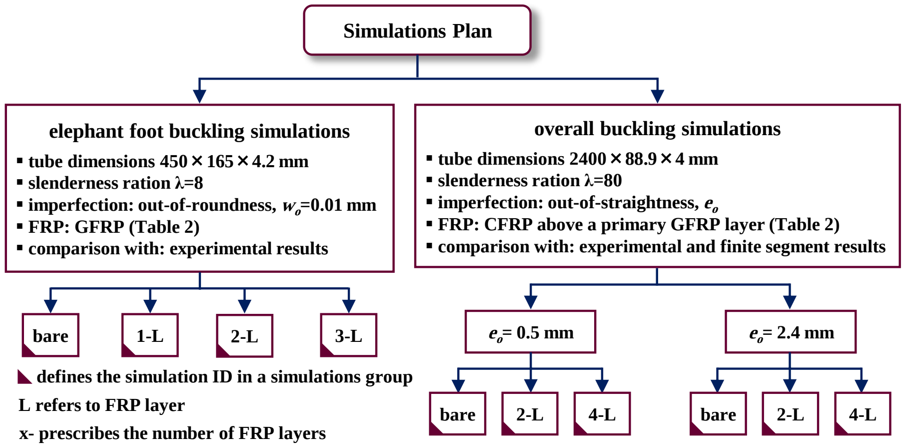

Fig. 1 The simulations tree

3. Simulations plan

Fig. 1 shows the simulations tree. Ten nonlinear large-deformations three-dimensional (3D) FEA were performed to simulate the two considered buckling modes. Four simulations were conducted to investigate the elephant foot buckling. The four simulations include a bare tube and three GFRP-strengthened tubes with 1, 2 and 3 layers. The finite element results were compared with the experimental results of Teng and Hu (2007). Two out-of-straightness values (e_o= 0.5 and 2.4 mm) were investigated through three simulations (a bare tube and two CFRP-strengthened tubes with 2 and 4 layers) for each studied e_o. The finite element results of e_o=0.5 mm and e_o=2.4 mm were compared with the experimental and numerical (finite segment method) results, respectively, of Gao *et al.* (2013). It is worth mentioning that the exact e_o value of tested tubes is not known, and therefore e_o=0.5 mm is an assumption and not simulating the real tested specimens accurately.

4. Finite element analysis (FEA)

ANSYS 14 software (ANSYS, Inc. 2011) has been used to perform 3D nonlinear FEA analysis for the reviewed experiments in section 2 in order to simulate the two studied buckling modes.

4.1 Element type and material

The steel tubes were modelled using two shell element alternatives; 4-nodes (SHELL181) and 8-nodes (SHELL281) as shown in Figs. 2-a and 2-b, respectively. Both elements are suitable for large strain nonlinear analysis of thin to moderately thick shell structures. Each node has six degrees of freedom (three translations and three rotations). Membrane option reduces the degree of freedom to three translations at node and neglects the bending stiffness. Although all applied forces are in-plane, the imperfections and buckling shapes are out-of-plane. Therefore, membrane option was not activated in order to provide reliable general analysis. Although SHELL281 is more suitable for curved shells similar to the studied tubes, performed simulations (for each considered buckling mode) have shown approximately identical results for both elements (SHELL181 and SHELL281). Therefore SHELL181 was recommended to save the computation time. It is very important to activate the full integration with incompatible modes option and not to use the default option of reduced integration with hourglass control for all the presented simulations. SHELL181 uses the method of incompatible modes by adding bubble type shape functions to the formulation that gives specific form of SHELL181 with much better bending performance. The full integration (2×2 quadrature) must be used when including the incompatible modes in the analysis. In order to highlight the importance of this option, all the simulations were repeated with reduced integration instead of the current choice. The results were very poor representation for the inward buckling in elephant foot simulations, and there was divergence of the solution in few simulations unlike the presented research in this paper. Elasto-plastic material was defined for simulating the steel. Young's modulus was set according to Table 1 whereas poisson's ratio was set to 0.3. The plasticity parameters will be introduced in section 4.5.

BEAM188 element (Fig. 2-c) was used to simulate the FRP for both the studied buckling modes (refer to Figs. 3-4). The beam axis will coincide with the 0º direction of FRP. This means that the minor stiffness of 90º direction

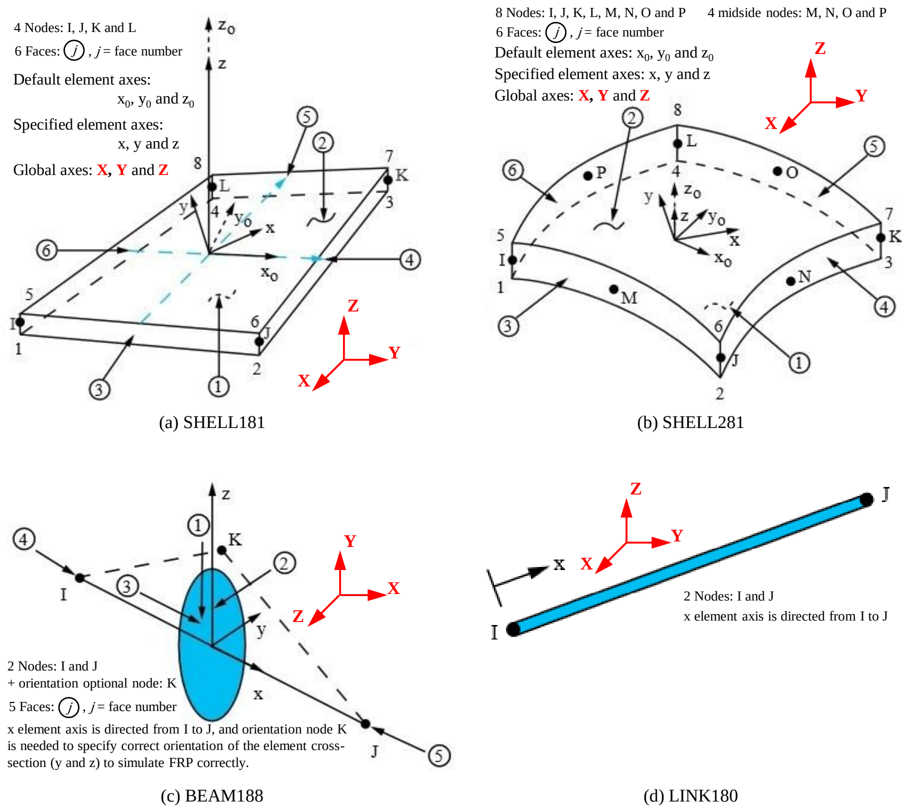

Fig. 2 The finite elements (ANSYS, 2011) used to model the steel tubes, FRP and the conical caps

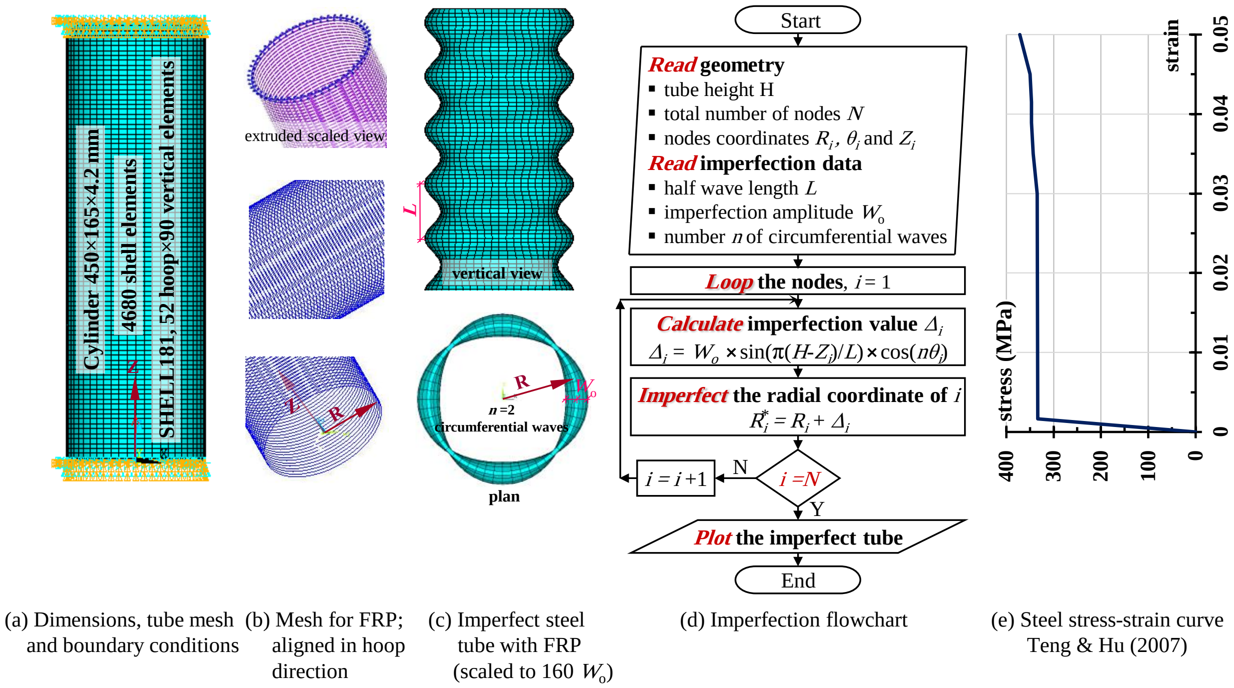

Fig. 3 The finite element model and data for the elephant foot buckling simulations

was ignored in the analysis. BEAM188 has two nodes with six degree of freedom at each node (three translations and three rotations). Also, BEAM188 supports orientation optional node K (Fig. 2-c). FRP was defined as an elastic material similar to its behavior. The Young's modulus was set according to Table 2.

LINK180 element (Fig. 2-d) was used to form the conical links simulating the rigid hinge at tube ends (Fig. 4-a). LINK180 is 3D truss element with two nodes. Each node has three translational degrees of freedom. Elastic material with large value of Young's modulus was defined for these caps to eliminate their axial deformation.

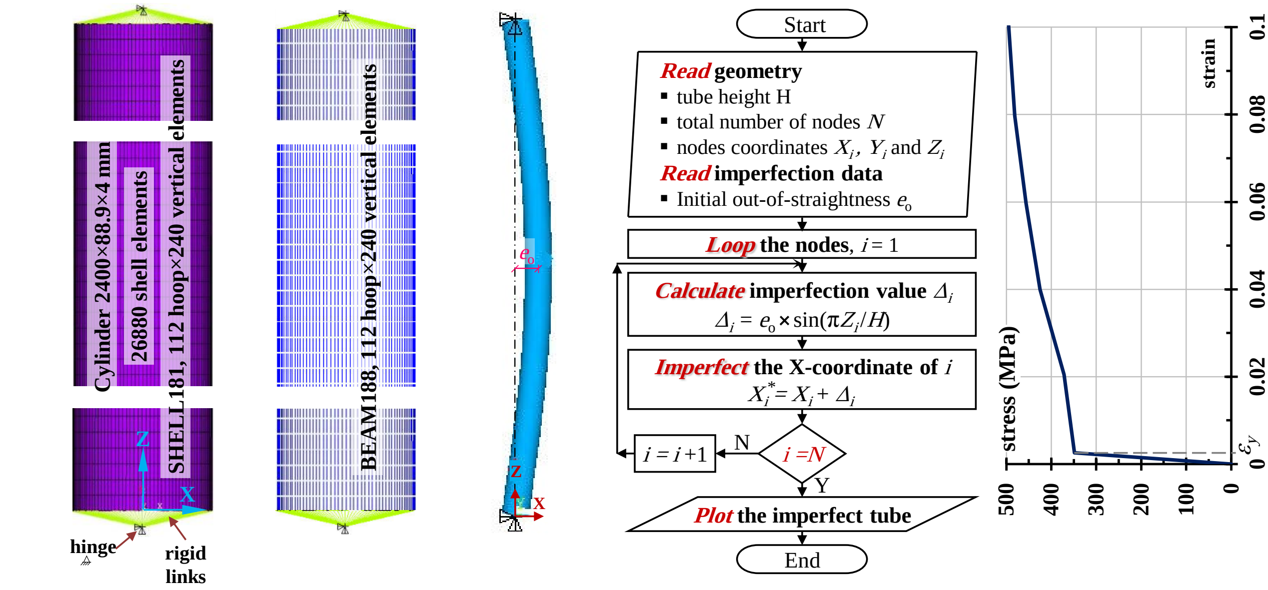

(a) Dimensions, tube mesh and boundary conditions (b) Mesh for FRP; aligned in vertical direction (c) Imperfect steel tube with FRP (scaled to $8e_o$) (d) Imperfection flowchart (e) Steel stress-strain curve

Fig. 4 The finite element model and data for the overall buckling simulations

4.2 Meshing and cross-sections

The shell element sizes (circumference×vertical) were set equal to 10×5 mm and 2.5×10 mm for elephant foot and overall buckling models, respectively. The longer dimension (10 mm) was aligned in the hoop direction for the elephant foot buckling study because the number of waves in circumferential direction was small unlike the vertical direction. However, it was aligned in the vertical direction for the overall buckling study to decrease the element number through the vertical direction (2400 mm). Figs. 3-a and 4-a illustrate the steel tube models of the elephant foot and overall buckling simulations, respectively. Uniform shell thickness of 4.2 and 4 mm was defined for the elephant foot and overall buckling tubes, respectively.

The FRP beam elements were aligned with the shell joints in circumference direction for elephant foot study, and in vertical direction for overall buckling study. Whereas the beam length was 10 mm constant for both simulations, the beam width was set equal to 5 and 2.5 mm, for the elephant foot and overall buckling simulations, respectively. The thickness was set equal to that of FRP given in Table 2 times the number of layers in addition to the equivalent thickness representing the overlap length averaged over the perimeter. For the overall buckling simulations, the thickness of GFRP primary layer was replaced with equivalent CFRP thickness according to Young's modulus ratio. The orientation node was defined for BEAM188 to orient the cross section properly (the width and thickness must be tangent and perpendicular to the tube surface, respectively). Figs. 3-b and 4-b illustrate the FRP meshing for the elephant foot and overall buckling simulations, respectively.

The length of link elements was equal to the geometric distance between the cap vertex and the joints of the corresponding tube end as shown in Fig. 6-a. The link cross-section area was set to a large value to provide rigid non-deformable links.

4.3 Boundary conditions and loading

For the elephant foot buckling models, the top and bottom ends were fully restrained (translations and rotations) except the axial translation of the top end which was left unrestrained to allow the application of load. Axial displacement of 5, 11, 13 and 15 mm was applied at the top end of the bare, 1-L, 2-L and 3-L tubes, respectively. Details of loading sequence will be presented in section 4.5.2.

For overall buckling models, rigid conical caps were added on the two ends as shown in Fig. 4-a to simulate the hinge behavior. These caps consist of rigid links connecting the edge joints with the cone vertex. The translations (not the rotations) at the cone vertex were restrained to represent the hinge behavior. Axial shortening of 6 mm was applied at the apex of the upper conical cap in small increments to track the overall buckling deformation and to detect the buckling load. Details of loading sequence will be presented in section 4.5.3.

4.4 Geometric imperfections

The loading on the tubes is perfectly axial and is resisted by the membrane stiffness. Therefore, out-of-plan imperfections (perturbations) are necessary to initiate the out-of-plan deformations and to guide to the desired buckling shape. For the elephant foot buckling models, non-axisymmetric imperfection was applied for all the simulated tubes. This initial geometric imperfection guides the tube to the expected outward and inward buckling. Fig. 3-c illustrates the imperfect strengthened tube after

Table 3 The nonlinear preferences of the presented simulations

	Elephant foot buckling simulations	Overall buckling simulations	Section
Integration scheme	full integration with incompatible modes	full integration with incompatible modes	4.1
Solution of nonlinear equations	arc-length method	full Newton-Raphson method	4.5.1
Loading	5-15 mm (refer to Table 4)	6 mm (refer to Table 5)	4.5.2-3
Automatic load stepping	arc-length procedure (Table 4)	ON for e_o=0.5 mm simulations OFF for e_o=2.4 mm simulations	4.5.3
Limits for controlling the iterations and bisection of substeps			4.5.4
Iterations number per substep (NEQIT)	200	100	
Prediction of the number of iterations per substep	ON	ON	
Effective plastic strain increment $\Delta\bar{\varepsilon}_p$	1%	1% (2%)*	
Upper limit of arc-length	0.25-1.50 mm (Table 4)	------	
Maximum vertical displacement Δu_Z	5-15 mm (Table 4)	------	
Convergence criteria			4.5.5
criterion	force and (moment)	displacement	
norm	2	2	
tolerance	5%	0.01% (0.1%)*	
minimum reference	600 kN (200 kN.m)	------	
minimum criterion	30 kN (10 kN.m)	------	
Termination criteria in case of non-convergence			4.5.6
reaching the cumulative iterations number	25,000	1000	
reaching both the minimum size of load increment and NEQIT	0.0013-0.005 mm (Table 4)	0.20-0.025 mm (Table 5)	

*for the bare-e_o =0.5 simulation in which more inelastic deformation and convergence difficulties are expected.

imposing imperfections according to the formula $\Delta_i = w_o \sin(\pi(450 - Z_i)/L) \times \cos(n\,\theta)$ given by Teng and Hu (2007). The procedure of applying the imperfection and the definitions of Δ, w_o, H, L, θ, and n are given in Fig. 3-d. The imperfection amplitude w_o, the half wave length of imperfection in vertical direction L, and the number of circumferential waves of imperfections n were set equal to 0.01, 31.75 and 2, respectively.

For the overall buckling models, out-of-straightness (initial imperfection e_o) in the form of simple half sine wave $\Delta_i = e_o \sin(\pi Z_i / L)$ was applied for all simulated tubes. Figs. 4-c and 4-d illustrate the imperfect tube and the procedure of applying imperfections, respectively. Two values of e_o were investigated, 0.5 and 2.4 mm.

4.5 Nonlinear buckling analysis

Nonlinear large deflection static analysis with fine load increments was employed to track the deformation of the simulated tubes. Von Mises yield criterion and multi-linear isotropic hardening material model was adopted to represent the steel plastic deformation given in Figs. 3-e and 4-e, respectively, for the elephant foot buckling and the overall buckling simulations. The values of the yield stress and ultimate stress were introduced in Table 1 for the two tested steel types. For large deflection analysis (NLGEOM, ON), ANSYS formulates the consistent stiffness matrix for all used elements to enhance the convergence of nonlinear analysis. Again, it is worth mentioning that the full integration with incompatible modes option of SHELL181 is necessary in order to enhance the bending deformation as discussed in section 4.1.

4.5.1 Solution of nonlinear equations

In most of the available FEA softwares, Newton-Raphson method is the default for the solution of nonlinear equations because of its quadratic convergence rate. However, it is not without limitations. In post-buckling analysis phase, Newton-Raphson method may fail to accurately track the load-displacement curve when the load value remains unchanged or decreases with continuous increasing deformation. Using displacement-controlled loading can circumvent (in many cases) this drawback for overall buckling simulations. For more sophisticated buckling problems comprising snap-through and snap-back instabilities, the arc-length method becomes a better choice as it causes nonlinear iterations to converge along an arc and prevents the divergence even if the slope is zero (or negative). Thereby, the arc-length method was the proper choice to simulate the elephant foot buckling. Table 3 summarizes the preferences of the presented nonlinear analyses for both elephant foot and overall buckling conducted simulations.

Table 4 The loading procedure using Arc-length method for the elephant foot buckling simulations

	bare	1-L	2-L	3-L	Comment
Total displacement loading (mm)	5*	11*	13*	15*	set on the top end of the tube; refer to Figs. 3-4.
Preliminary number of load increments (substeps); NSBSTP	20	338	100	100	ANSYS input to estimate the initial (reference) arc-length.
MAXARC	1	25	10	10	ANSYS input to adjust the arc-length factor.
MINARC	0.02	0.1	0.001	0.001	ANSYS input to adjust the arc-length factor.
The size of first load increment	0.2	0.0325	0.13	0.15	reference arc-length = total load/NSBSTP
The size of maximum load increment (mm); upper limit of the arc-length	0.25	0.8125	1.3	1.5	MAXARC×reference arc-length the substep is bisected if this limit was exceeded.
The size of minimum load increment (mm); lower limit of the arc-length	0.005	0.00325	0.0013	0.0015	MINARC×reference arc-length the solution terminates if this limit was violated

* the same value was prescribed as a displacement limit.

Table 5 The loading procedure using the full Newton-Raphson method for the overall buckling simulations

	e_o=0.5 mm simulations			e_o=2.4 mm simulations			
	bare	2-L	4-L	bare	2-L	4-L	Comment
Total displacement load (mm)	6	6	6	6	6	6	set on the apex of the top cap (Fig. 4-a)
Automatic load stepping	ON	ON	ON	OFF	OFF	OFF	
Preliminary number of load increments (substeps);NSBSTP	120	120	120	30	30	30	ANSYS input to control the loading and to estimate the first load increment
Maximum number of load increments (substeps); NSBMX	240	240	240	30	30	30	ANSYS input to control the loading, the iterations and termination of solution.
Minimum number of load increments; NSBMN	30	30	30	30	30	30	ANSYS input to control the loading and the iterations procedure.
The size of the first load increment (mm)	0.05	0.05	0.05	0.2	0.2	0.2	total load/NSBSTP
The size of the maximum load increment (mm)	0.2	0.2	0.2	0.2	0.2	0.2	total load/NSBMX
The size of the minimum load increment (mm)	0.025	0.025	0.025	0.2	0.2	0.2	total load/NSBMN the solution terminates if this limit was violated

4.5.2 Loading for the elephant foot buckling simulations (Arc-length method)

The procedure of controlling the load is given in Table 4. In the first increment, ANSYS calculates the reference arc length equal to the prescribed displacement divided by the given total number NSUBST of increments (substeps); for example 15/100=0.15 mm for 3-L simulation. Subsequently, a new arc-length is calculated for each substep based on that of the previous substep. ANSYS uses two multipliers MINARC and MAXARC to adjust the recent calculated arc length within upper limit (MAXARC× reference arc length) and lower limit (MINARC×reference arc length). For example, setting MAXARC and MINARC to 10 and 0.001, respectively, for 3-L simulation will provide a loading range of 1.5-0.0015 mm for the increments subsequent to the first 0.15 mm increment. More interpretation for the concept of setting the arc-length parameters will be explained in section 5.1 in view of the results.

4.5.3 Loading for overall buckling simulations (Newton-Raphson method)

Typical axial shortening of 6 mm was applied for all the six tubes. For the three imperfect tubes with e_o of 0.5 mm, the automatic time stepping was urgent (AUTOTS, ON) because of the small imperfection value which makes the tubes structural behavior sensitive to the applied displacement loading besides the presence of significant inelastic deformation from the beginning of the simulation. The automatic time stepping comprises an internal algorithm that enables ANSYS to ensure that the load increment size is neither too large nor too small. Also, it predicts the size of the increment based on the number of iterations, imminent yield of elements, and equivalent plastic strain increment in the preceding load increment. The first load increment was 0.05 mm with factorization range from 0.5 to 4 (0.025-0.2 mm) for subsequent increments. On the contrary, constant thirty increments of 0.2 mm displacement loading were acceptable to achieve the total load (6 mm) without divergence for the other three tubes whose e_o is 2.4 mm. The load increments data for the six overall buckling simulations are given in Table 5.

4.5.4 Control of the iterations and bisections

ANSYS provides automatic cutback procedure (with many criteria) to reduce the size of the load increment to overcome the convergence difficulties (if any) during the nonlinear analysis. Table 3 lists and defines the prescribed criteria for both elephant foot and overall buckling simulations. The load increment (substep) is automatically bisected when any prescribed limit (criterion) is violated. The specified plastic strain limit of 1% is very important to perform such complicated nonlinear buckling analysis comprising significant plastic deformation. It is worth mentioning that the ANSYS default is 15% which is extremely large and does not lead to a converged solution or correct deformations in the considered problems.

4.5.5 Convergence criteria

Table 3 defines the convergence criteria for the conducted simulations. The convergence criteria should be carefully set for each buckling analysis, otherwise a converged solution and a correct deformation may not be possible. Moreover, setting the convergence criteria inappropriately may result in extremely long computation time which is needless.

For elephant foot buckling simulations (arc-length method), force and moment convergence criteria with norm 2 were set. The tolerance was set to 5%. The default minimum reference (0.01) was replaced with 600,000 N for the force criterion and 200,000,000 N mm for the moment criterion. These values are reasonable because of the considered units (N and mm) in the models. Based on the previous data, the maximum limit for the residual norm will be 30 kN for the force criterion and 10 kN m (1.0 ton m) for the moment criterion (or 5% of the reaction norm which greater). Re-writing in view of the 52 nodes forming the tube end, the minimum reference for the force and moment per every reaction node will be approximately equal to 0.58 kN and 0.19 kN m, respectively. These limits are, appropriately enough, to perform correct analysis.

For the overall buckling simulations (Newton-Raphson method), the displacement criterion was suitable for such simply supported (no moment reaction) tubes that experiencing large deformation. The norm 2 was used to represent all the nodes. Rigorous tolerance of 0.01% was set for all the simulations except the bare-e_o=0.5 tube whose tolerance was slightly released for convergence purpose.

4.5.6 Analysis termination criterion

The nonlinear analysis ends successfully when the prescribed load is fully analyzed within the prescribed convergence limits. There should be criterion for stopping the analysis if the solution does not converge in order to adjust the input parameters. The termination criterion is shown in Table 3. It is worth mentioning that all the presented analyses were successfully completed.

5. Results

Table 6 lists the number of actually executed load increments, iterations and bisections for all the presented simulations.

For the elephant foot buckling simulations, Tables 7 and 8 declare the increment of axial shortening and the restraint of deformation, respectively, for the strengthened tubes compared with the bare one. Figs. 5 and 6 illuminate the deformations, and the load-axial displacement histories, respectively, compared with the experimental results.

For the overall buckling simulations, Figs. 7 and 8 show the displacement histories of e_o =0.5 and e_o=2.4 mm tubes, respectively, compared with the corresponding results of Gao *et al*. (2013). Fig. 9 illuminates the deformation and propagation of the plastic strain. Fig. 10 demonstrates the axial strain variation for at the mid-height of the tubes compared with the corresponding experimental results.

5.1 Elephant foot buckling simulations

The total number of increments, the total number of bisections, and the total cumulative number of iterations are significantly increased with the increase of confinement by adding a new FRP layer according to Table 6. It could be argued that the significant propagation of inward deformation for 2-L and 3-L simulations (Fig. 5) magnified the gap between 1-L and 2-L simulations (101 to 1388, 68 to 1336 and 655 to 20045 for the increments, bisections and total iterations numbers, respectively). This observation coincides with the reduction of the lower limit of the arc-length with the increase of confinement (number of FRP layers) as shown in Table 4. The smaller lower limit of the arc-length allows extremely fine load increments (starting approximately from the middle of simulation) to track the reversible radial displacement (turn from outward "yellow" to inward "blue" as Fig. 5 displays). Also, this coincides with the monitored violated bisection limits (Table 6) which show that the maximum arc-length was the predominated

Table 6 The number (N^o) of actual executed load increments, iterations and bisections

	Elephant foot buckling simulations				Overall buckling simulations					
					e_o=0.5 mm simulations			e_o=2.4 mm simulations		
	bare	1-L	2-L	3-L	bare	2-L	4-L	bare	2-L	4-L
Total N^o of load increments	44	101	1,388	1,742	33	33	38	30	30	30
Maximum iterations N^o per increment	4	9	186	50	15	44	14	15	12	6
Total N^o of bisections	35	68	1,336	1,705	-----	-----	3	-----	-----	-----
Total N^o of cumulative iterations	227	655	20,045	22,670	88	167	480	101	142	132
Limits violated to cause bisections in descending order according to the violating N^o.	1- $\Delta\bar{\varepsilon}_p$ 2-upper limit of arc-length		1-upper limit of arc-length 2- ΔU_z 3- $\Delta\bar{\varepsilon}_p$ 4-NEQIT		-----	-----	NEQIT	-----	-----	-----

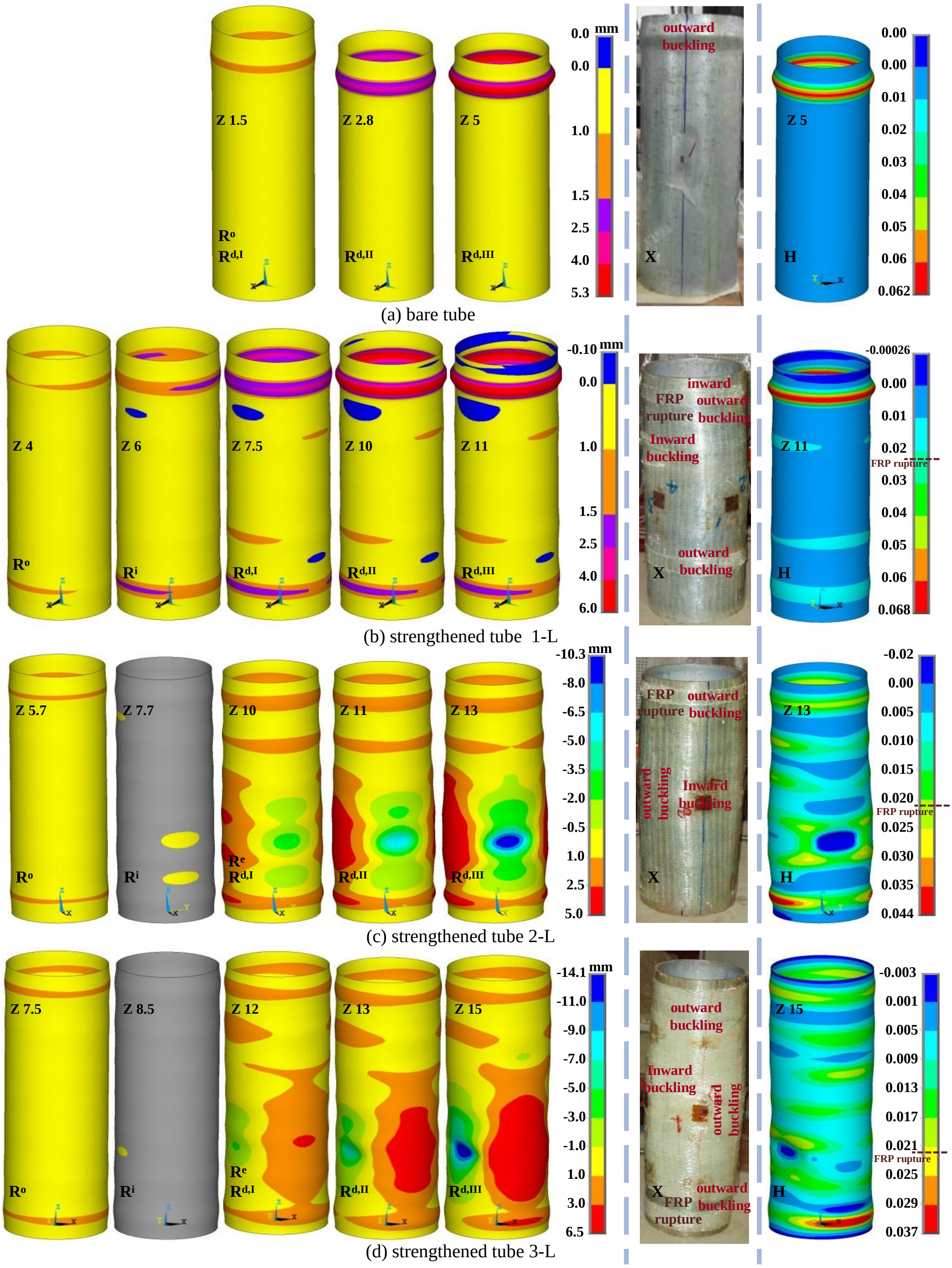

R Radial displacement (outward is + "yellow to red" & inward is – "lemon to blue")
X Experimental deformed shape (Teng & Hu, 2007)
H Hoop strain, all colors are tensile except blue (if any) representing compressive strain
Z Value of axial shortening (Uz) in mm at which this deformation was captured
o initiation of localized outward buckling (+ exceeded 1 mm)
i initiation of inward buckling (-ve out-of-plane deformation initiation)

e equality of both max. outward and max. inward deformations
d development of excessive buckling along the descending part of the load displacement curve (Fig. 6)
I at the start zone of the descending curve
II in the middle zone of the descending curve
III at the end zone of the descending curve

Fig. 5 Deformation of the elephant foot buckling tubes; initiation and propagation of the out-of-plane buckling and plastic strain (plotted on deformed shape; scale factor 1.5-2)

Table 7 The axial shortening increment (buckling delay) for the strengthened elephant foot buckling tubes

		bare	1-L	2-L	3-L
Axial shortening at ultimate load (before the descending part)	*mm*	0.8	7	11	12
	%		775	1,275	1,400
Axial shortening at localized outward buckling initiation[1]	*mm*	1.5	4	5.7	7.5
	%		167	280	400
Axial shortening at localized inward buckling initiation	*mm*	----	6	7.7	8.5
	%			28	42

- * underlined value is the reference for % calculations.
- % indicates the percentage of the increment compared with the reference value.
- [1]outward buckling exceeded 1 mm in a local ring.

Table 8 The constraint of deformation for the strengthened elephant foot buckling tubes

Maximum deformation type	*Uz* mm	absolute or %	bare	1-L	2-L	3-L
Tensile hoop strain	5	absolute	0.062	0.017	0.012	0.009
		%		-73	-81	-85
	13	absolute	----	0.082	0.044	0.030
		%			-46	-63
Outward buckling (mm)	5	absolute	5.341	1.44	0.901	0.816
		%		-73	-83	-85
	13	absolute	----	7.35	5.058	4.327
		%			-31	-41
Inward buckling (mm)	13	absolute	----	0.288	10.296	7.211
		%				-30

- * underlined value is the reference for % calculations.
- % indicates the percentage of the decrement compared with the reference value

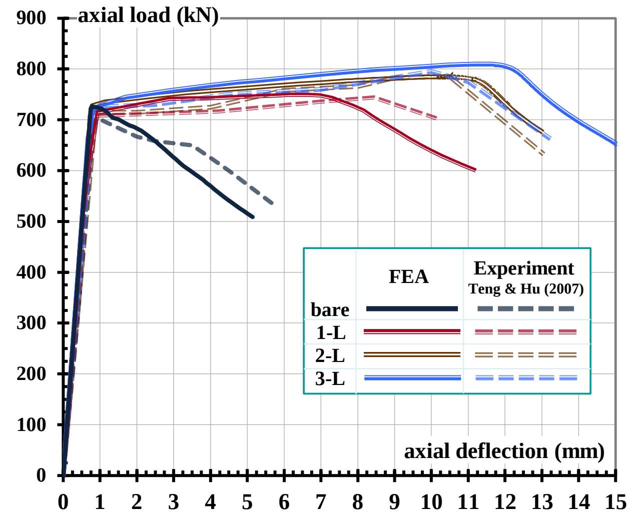

Fig. 6 The load-axial displacement curves for the simulated elephant foot buckling tubes

reason for bisection in 2-L and 3-L simulations. On the contrary, the upper limit of arc-length is increased with the increase of confinement as evident in Table 4. This contradiction can be interpreted in view of plastic strain propagation (Fig. 5 and Table 8). The increment of FRPlayers number reduces the plastic strain propagation especially in the beginning of the simulation (before the inward buckling initiation) and therefore, it allows higher upper limit for the arc-length. Again, this new observation was confirmed with the monitored violated bisection limits (in Table 6) which show that the plastic strain increment is the predominant reason for bisection in the bare and 1-L simulations (lower confinement and higher plastic strain flow), and a secondary reason for 2-L and 3-L simulations (higher confinement and lower $\Delta\bar{\varepsilon}_p$) as shown in Fig. 5 and Table 8. The violated bisection limits (either $\Delta\bar{\varepsilon}_p$ for the first two simulations or the maximum arc-length for the last two simulations) were observed intensively on the descending part of the load displacement curves.

5.1.1 Ultimate load and deformation

Figs. 5 and 6 show high consistency between the results of both the presented FEA and Teng and Hu (2007) experiments. The percentage of error in the estimated ultimate load was 3.21%, 0.75%, 0.03% and 1.87% for the bare, 1-L, 2-L and 3-L simulations, respectively, compared with the experimental results. The increment in load capacity (compared with the bare simulation) was minor and approximately equal to 3.7% for each extra FRP layer unlike the significant improvement in ductility as revealed by the experimental results (Teng and Hu 2007).

The deformation consistency between the FEA and the experimental results is obvious in Fig. 5. The outward buckling is formed near the tube ends, and is more noticeable in the bare and 1-L simulations unlike the inward buckling which is more noticeable in the 2-L and 3-L simulations. Table 7 and Fig. 6 show that adding only one FRP layer results in 775% increase in the axial shortening (at the ultimate load), and that adding one more layer results in additional 500% increase unlike the third layer which provides minor additional increase in axial shortening (125%).

The presented FEA shows advantages over the experimental results. FEA made it possible to capture the localized outward bulge initiation, and the subsequent inward buckling initiation if any. Fig. 5 shows the captured deformations at these two successive stages (R^o and R^i). Table 7 reveals that the increment in axial shortening before R^o stage (suspension of outward localization) has linear relationship with FRP layers number, and approximately equal to 133% (compared with the bare tube) for each extra layer. However, the increment in axial shortening before R^i stage (suspension of inward buckling initiation) was slightly smaller compared with that of R^o, and moreover it is decelerated with adding extra FRP layer according to the monitored results in Table 7. Besides the determination of the buckling initiations, FEA made it possible to estimate the constraint in the hoop strain and the out-of-plane deformation for each extra FRP layer as given in Table 8. Adding the first FRP layer reduces the tensile hoop strain and the outward deformation with about 73% (compared with the bare tube) but initiates the inward deformation.

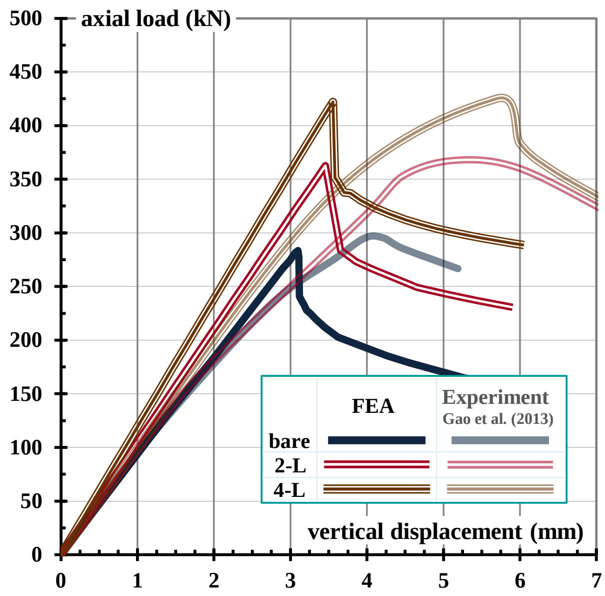

(a) load-axial displacement

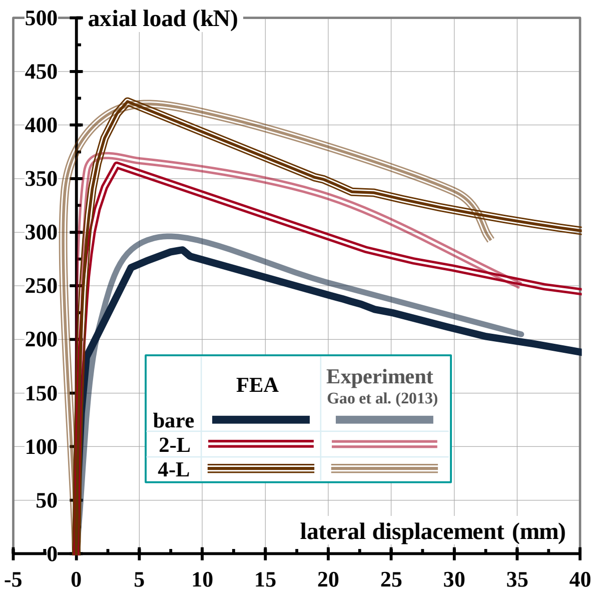

(b) load-lateral displacement

Fig. 7 The load-displacement histories for the overall buckling tubes with e_o=0.5 mm (FEA versus experiments)

Adding the second FRP layer increases slightly (with average 9%) the constraint on the tensile hoop strain and the outward deformation but magnifies the inward deformation to the extent that its magnitude exceeds the outward deformation. The third FRP layer constrains of the inward deformation and reduces it to about 30% (compared with 2-L simulation) in addition to the continuity of restraining the outward deformation. Another benefit of the provided FEA is the presentation of the hoop strain distribution (Fig. 5). It is noticeable that attaching FRP layers mitigates the hoop strain localization (concentration) at the ends and increases the uniformity of the distribution. Therefore, the FRP rupture at the ends is eliminated and more axial shortening could be sustained with the increase of FRP layers number. Finally, Fig. 5 presents explanation for the process of the buckling propagation. The process comprises three stages as follows; 1) the initiation of localized outward buckling R^o, 2) the initiation of inward buckling R^i if any, and 3) the development of excessive buckling R^d along the descending part of load displacement curves. The last stage is subdivided into three zones $R^{d,I}$, $R^{d,II}$ and $R^{d,III}$ at the start, middle and end of the descending curve, respectively. For 2-L and 3-L simulations, it was monitored that the absolute maximum of the inward deformation equalizes that of the outward deformation at $R^{d,I}$, and then it exceeds the outward deformation in the subsequent zones ($R^{d,II}$ and $R^{d,III}$). On the other hand, the 1-L tube has shown minor inward deformation (especially near the support) whereas it was absent in the bare simulation whose R^o stage starts at the ultimate load and coincides with $R^{d,I}$ stage.

Although the presented simulations assume no rupture of FRP and full contact between the FRP and the steel tube, the presented hoop strain and radial displacement distributions in Fig. 5 can overcome these limitations. The FRP rupture can be read in view of its ultimate strain (0.0228 as given in Table 2) which is marked with dash line on the hoop strain legend in Fig. 5. FRP rupture is expected at the circular strips (rings) that exhibit tensile hoop strain equal to (or higher than) the marked color of 0.0228 contour. Also, the delamination of FRP is expected at the extreme inward buckling spots where high inward deformation (compressive hoop strain) is localized and bounded with high outward deformation (tensile hoop strain). The elastic FRP material might not be flexible enough to follow such abrupt change from positive to localized negative deformation unlike the ductile steel material. It could be argued that the absence of the real imperfection data for the investigated tubes followed by the discussed two modeling limitations (no FRP rupture and the full contact with the steel) were the reasons for the noticeable small inconsistency of the descending part of load-displacement histories especially for 3-L simulation.

5.2 Overall buckling simulations

Table 6 shows that the number of load increments and iterations is slightly higher for e_o=0.5 mm simulations compared with those of e_o=2.4 mm simulations. This might be due to the higher flow of plastic strain in the tubes imperfect with smaller e_o compared with those with e_o=2.4 mm which exhibit more elastic buckling. The smoothness of the analysis is evident in the prescribed narrow range of the size of load increments (the maximum load increment size is eight times the minimum), and the no need to bisection of load increments in most of the simulations as Table 5 and 6, respectively, confirm. Only three bisections were needed for 4-L (e_o=0.5 mm) simulation in order to pick accurately the ultimate load of this stiff strengthened tube (four FRP layers and minor out-of-straightness). It could be argued that the relaxation in both the convergence criteria and the plastic strain increment limit for the bare simulation (e_o=0.5 mm) as given in Table 3 results in unexpected relatively smaller number of cumulative iterations as recorded in Table 6. It is worth mentioning that

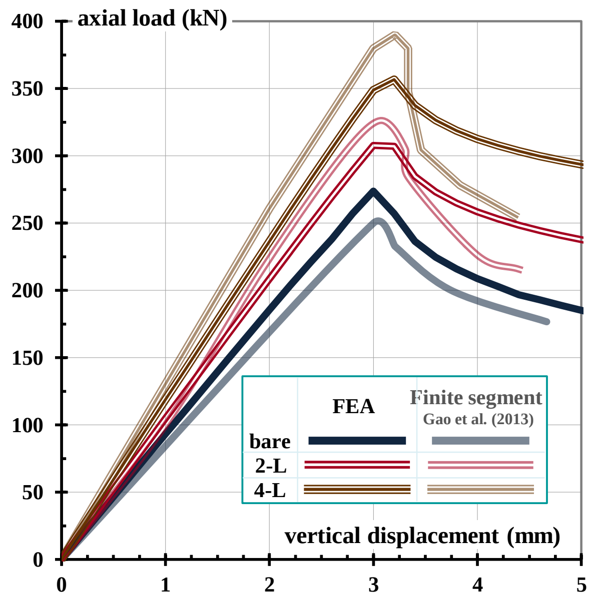

(a) load-axial displacement

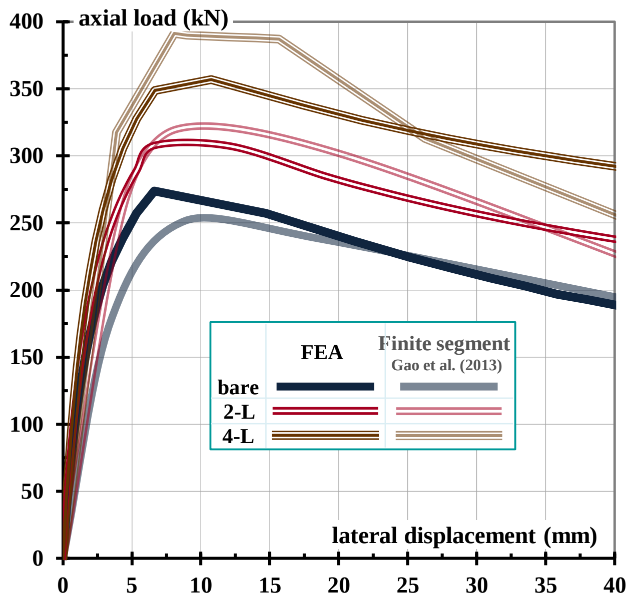

(b) load-lateral displacement

Fig. 8 The load-displacement histories for the overall buckling tubes with e_o=2.4 mm (FEA versus finite segment)

the smoothness of the overall buckling simulations compared with elephant foot simulations is confronted with the huge number of elements in overall bucking model (about six times that of elephant foot buckling model as shown in Figs. 3-4).

5.2.1 Ultimate load and deformation

Figs. 7-10 reveal good agreement between the presented FEA results and Gao *et al.* (2013) results. It is worth mentioning that the assumed value e_o=0.5 mm was determined after several numerical trials because there was no experimental measurements for the actual out-of-straightness in the real specimens tested by Gao *et al.* (2013).

Figs. 7 and 8 confirm that the increase of number of CFRP layers increases the ultimate load capacity and the stiffness with insignificant gain in the ultimate displacements. The two bare simulations resulted in overestimated stiffness and ultimate load (as FEA often does) with average error of 9.5% (for ultimate load) compared with Gao *et al.* (2013) results. On the contrary, the four simulations of the strengthened tubes resulted in under estimated ultimate load with average error of 4.1% compared with Gao *et al*. (2013) results. This might be back to aligning the BEAM188 elements of all FRP layers at the same distance (from the tube center) within the nodes of SHELL181 elements unlike the real successive FRP layers. The previous percentages and Figs. 7-8 reveal good agreement with the Gao *et al.* (2013) results except for the axial displacements of the three tubes with e_o=0.5 mm as Fig. 7-a shows. Similar inconsistency was clear in the results of the finite segment analyses of the bare and 2-L tubes provided by Gao *et al*. (2013) without declaring the e_o value (not shown in this paper). The displacement inconsistency observed in Fig. 7-a could be interpreted according to the following reasons: 1) there was no experimental measurements for neither the e_o values nor any other imperfection data, 2) there might be real imperfections of different types either material or geometric with different shapes and values for the considered six tubes, 3) there might be minor misalignment with different values in the test setup of the different tubes, 4) the tangent modulus of the tested steel (after the onset of the yield) is not given in the considered experimental study (Gao *et al*., 2013), and 5) the length of the cap has significant influence on the FEA results for given small e_o values.

Fig. 9 reveals the efficiency of the presented simulations. FEA made it possible to monitor the initiation and the propagation of the plastic strain. Fig. 9-d interprets the increase in ultimate load with the increase in the number of FRP layers. Adding FRP layer postpones the initiation of the plastic strain, reduces the maximum plastic strain magnitude, mitigates its localization in the mid-height of the tube, and increases the distribution area of the plastic strain along the tube height. Therefore, higher stiffness and ultimate load is reported for each extra FRP layer.

Also, Fig. 10 highlights the merits of the presented FEA compared with the available experimental results. The strains on the four quadrant points (S1, S2, S3 and S4) of the simulated tubes were monitored at mid-height and compared with those recorded experimentally. Fig. 10 demonstrates that the load-strain history might be divided into three stages or intervals as graphically shown on the FEA results. In the first stage, all the sides of the tube exhibit approximately equal increase in the compressive strains up to a certain load (150 kN for the bare tube and 75 kN for the strengthened tubes). In the second stage, the rate of increase in compressive strains becomes higher for S2 on the compression side and smaller for S4 on the tension side, whereas it continues with the same rate for the other two sides (S1 and S3). This behavior manifests significant elastic buckling in this second stage as the strains on the four sides of the tube become unequal. Unexpected observation is that the bifurcation load (the start of this

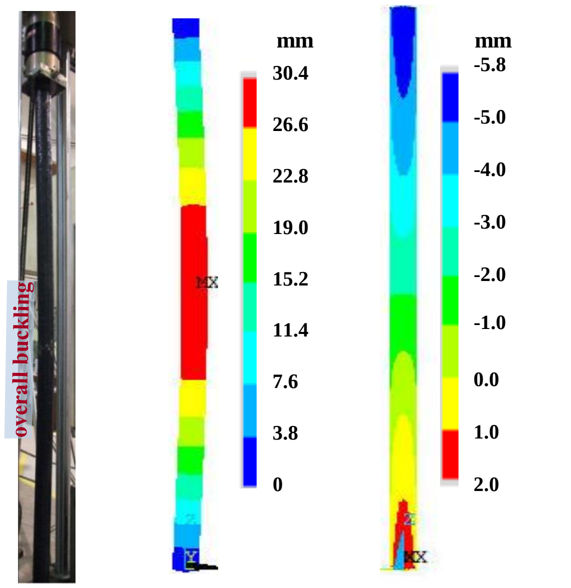

(a) Experiment Gao *et al.* (2013) (b) FEA – deformation & lateral displacement (c) FEA – vertical displacement

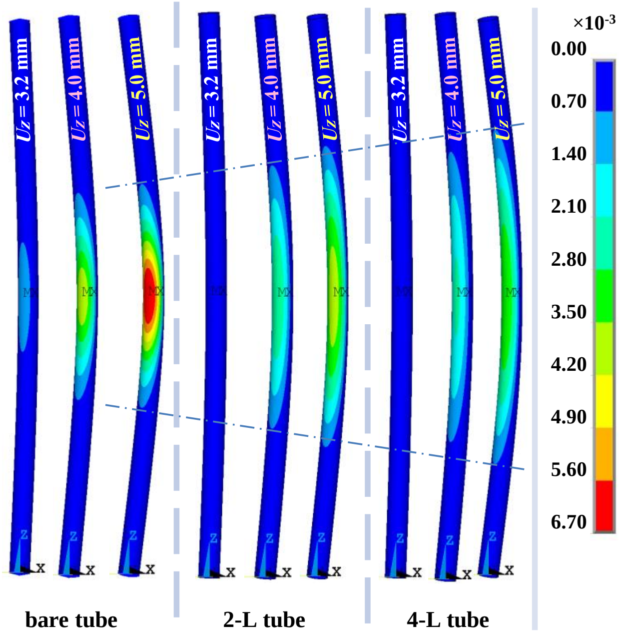

(d) FEA-initiation & propagation of equivalent plastic strain (plotted on deformed shape; scale factor 5)

Fig. 9 The deformation of the overall buckling tubes

second stage) was smaller for the strengthened simulation (75 kN) compared with that of the bare simulation (150 kN). This unexpected observation was also monitored in the available experimental histories. The interpretation for this observation is that the structural behavior of FRP in compression is different than in tension, and therefore strengthened tubes became more imperfect than the bare tube. This additional minor imperfection accelerated the start of stage 2. This stage continues until reaching the ultimate load point and before the steel material reaches its yield strain at approximately 0.17% on the compression side S2. Finally, the third stage represents the post-buckling behavior where the tube losses its stiffness, and the load capacity is reduced with excessive increase in compression strain on S2 side and cross over to tension on S4 side, whereas the compression strains on other sides (S1 and S3) exhibit insignificant increase. This last stage comprises steel inelastic buckling and Fig. 9-d shows its plastic strain propagation. Also, delamination and rupture of CFRP were observed experimentally on the compression side at compressive strain in the range 0.2-0.4%. The discrepancy between the tensile rupture strain limit (1.5%) and that observed experimentally (0.2 to 0.4%) for compressive strain confirms that the structural behavior of FRP is not similar for tensile and compressive loading. Any minor inconsistency between FEA and experimental results in Fig. 10 might be interpreted according to the five reasons mentioned in the comment on Fig. 7-a in additional to the two following reasons: 1) the delamination and rupture of FRP was not considered in the presented FEA, and 2) strain gage problems during the experimental measurement.

6. Conclusions

Tubular steel compression members may exhibit elephant foot buckling or overall buckling under extreme loading because of the existence of geometric imperfections (such as out-of-roundness and out-of-straightness) in additional to the steel material imperfections. In this study, seven steel tubes was strengthened with two types of FRP (GFRP and CFRP) to resist the two studied buckling types (elephant foot and overall). Three-dimensional nonlinear FEA was performed for the strengthened seven tubes as well as three bare references to investigate the structural behavior under monotonic compression loading. Several parameters were used to successfully complete the presented ten nonlinear simulations and correctly track the buckling behavior. The results were compared with the available experimental results (Teng and Hu 2007 and Gao *et al.* 2013). The following conclusions can be drawn.

- Strengthening steel tubular compression members with bonding FRP in the hoop direction for resisting the elephant foot buckling, and in the longitudinal direction for resisting the overall buckling results in significant improvement in ductility and strength, respectively.
- Full integration with incompatible modes procedure, adaptive load increments multipliers, suitable nonlinear procedures, and bisection limits especially for the plastic strain increment must be set properly to successfully track the buckling behavior.
- The elephant foot buckling simulations are more complicated compared to those of overall buckling because of the sudden localized change in out-of-plane deformation from outward to inward, and the higher intensity of the effective plastic strain.
- FEA results have showed many advantages in monitoring the deformation over the experimental studies.
- The FRP layers mitigate both the intensity and localization of the plastic strain at the outward bulged rings, and at the mid-height of the compression side of the elephant foot and overall buckling tubes, respectively. The equivalent plastic strain distribution becomes more uniform with the increase of the number of layers.

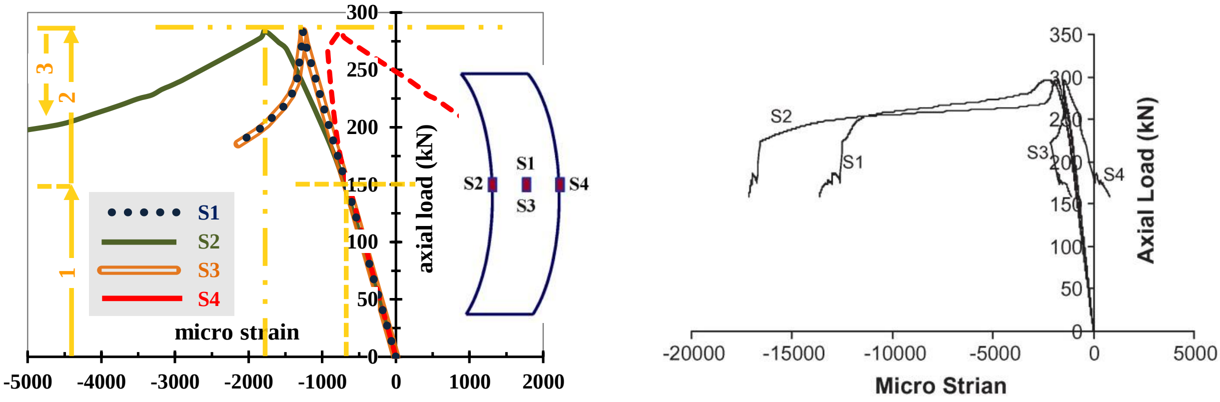

▪ FEA ▪ experimental (Gao *et al.* 2013)

(a) Reference bare tube

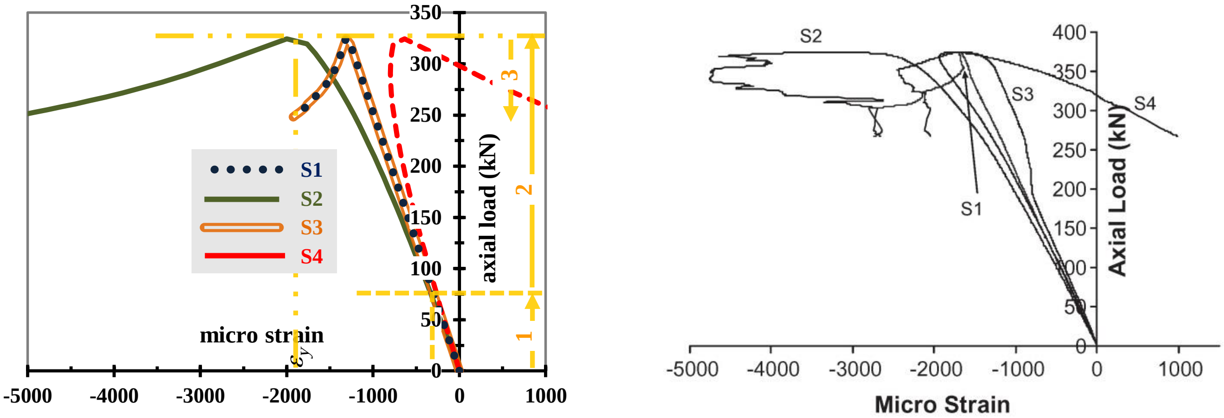

▪ FEA ▪ experimental (Gao *et al.* 2013)

(b) 2-L tube

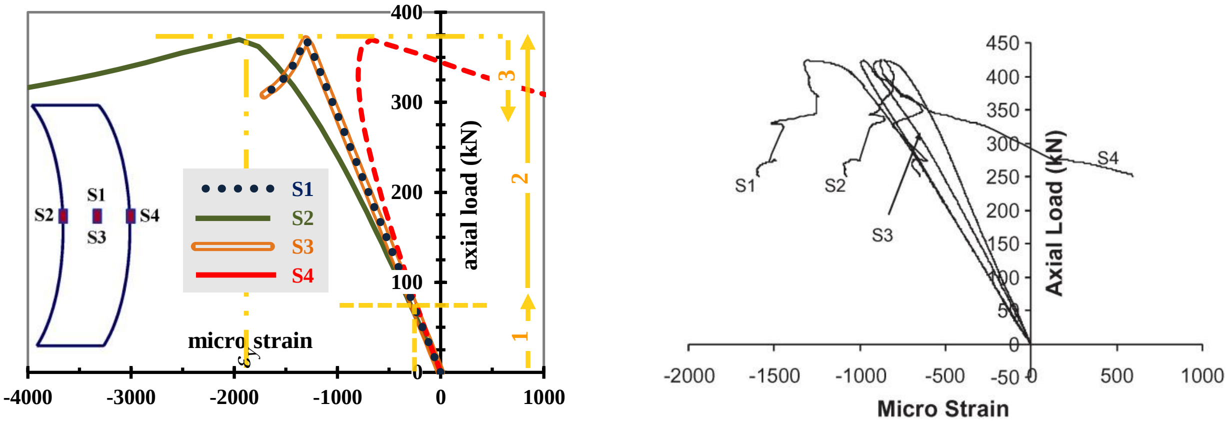

▪ FEA ▪ experimental (Gao *et al.* 2013)

(c) 4-L tube

Fig. 10 The variation of axial strain with axial load for the overall buckling tubes (FEA versus experiments)

- The elephant foot buckling was interpreted into three stages; initiation of localized outward buckling, initiation of inward buckling if any, and finally development of excessive buckling along the descending part of the load-displacement curve. Although adding extra layer postpones the three buckling stages, the first FRP layer initiates the second stage (inward buckling).
- The inward buckling is more noticeable for the steel

tubes strengthened with two layers and more, it becomes equal to the outward deformation at the start of the descending part of the load-displacement curve, and thereafter shows successive intensive increase along the descending curve.

- The overall buckling was interpreted into three stages; equal increase rate for compressive strains on the four sides of the tube, elastic buckling initiation and propagation with gradually increasing rate for the compressive strain on the compression side up to reaching the ultimate load at the yield strain, and finally the initiation of plastic strain with successive inelastic buckling and loss of strength. The second stage starts earlier in the strengthened tubes compared with the bare steel tube because of the existence of FRP layers which add minor geometry imperfection due to the dissimilarity of its tensile and compressive structural behavior.
- The assumptions of full contact between the steel and FRP, and the no rupture of FRP have limited drawbacks for the presented simulations compared with the computational time saving. However, including the epoxy resin interface and the FRP rupture in the simulations will provide more reliable results.
- The fact that different meshes and different imperfections may result in minor changes in the ultimate load, the displacements, and the local buckling locations does not change the proposed interpretation for the local and overall buckling phenomena.

References

ANSYS, Inc. (2011), ANSYS Structural Analysis Guide – Release 14, SAS IP, Inc., Southpointe, Canonsburg, PA, USA.

Avcar, M. (2014), "Elastic buckling of steel columns under axial compression", *American J. Civil Eng.*, **2**(3), 102-108. https://doi.org/10.11648/j.ajce.20140203.17.

Batikha, M., Chen, J.F., Rotter, J.M. and Teng, J.G. (2009), "Strengthening metallic cylindrical shells against elephant's foot buckling with FRP", *Thin-Walled Struct.*, **47**(10), 1078-1091. https://doi.org/10.1016/j.tws.2008.10.012.

Bukovska, P. and Karmazinova, M. (2012), "Behaviour of the tubular columns filled by concrete subjected to buckling compression", *Procedia Eng.*, **40**, 68-73. https://doi.org/10.1016/j.proeng.2012.07.057.

Chen, J.F., Rotter, J.M. and Teng, J.G. (2006), "A simple remedy for elephant's foot buckling in cylindrical silos and tanks", *Adv. Struct. Eng.*, **9**(3), 409-420. https://doi.org/10.1260/136943306777641968

Dundu, M. (2012), "Compressive strength of circular concrete filled steel tube columns", *Thin-Walled Struct*, **56**, 62-70. https://doi.org/10.1016/j.tws.2012.03.008.

El-Kholy, A.M., Morsy U.A. and Mourad, S.A. (2014), "Imperfection modeling using finite element approach with particular discretization", *J. Struct. Eng. (ASCE)*, **140**(7), P. http://dx.doi.org/10.1061/(ASCE)ST.1943-541X.0000950.

Gao, X.Y., Balendra, T. and Koh, C.G. (2013), "Buckling strength of slender circular tubular steel braces strengthened by CFRP", *Eng. Struct.*, **46**, 547-556. https://doi.org/10.1016/j.engstruct.2012.08.010.

Ghaemdoust, M.R., Narmashiri, K. and Yousefi, O. (2016). "Structural behaviors of deficient steel SHS short columns strengthened using CFRP", *Construct. Build. Mater.*, **126**, 1002-1011. https://doi.org/10.1016/j.conbuildmat.2016.09.099.

Moradi, M., and Arwade, S.R. (2014), "Improving buckling response of the square steel tube by using steel foam", *Struct. Eng. Mech.*, **51**(6), 1017–1036. https://doi.org/10.12989/SEM.2014.51.6.1017.

Narmashiri, K. and Mehramiz, G. (2016), "Strengthening of steel hollow pipe sections subjected to transverse loads using CFRP", *Struct. Eng. Mech.*, **60**(1), 163–173. https://doi.org/10.12989/SEM.2016.60.1.163.

Nishino, T. and Furukawa, T. (2004), "Strength and deformation capacities of circular hollow section steel member reinforced with carbon fiber", *Proceedings of 7th Pacific Structural Steel Conference (American Institute of Steel Construction)*, CA, USA, March.

Ohga, M., Takaue, A., Shigematsu, T., and Hara, T. (2001). "Effects of initial imperfections on nonlinear behaviors of thin-walled members", *Struct. Eng. Mech.*, **11**(5), 519–534. https://doi.org/10.12989/SEM.2001.11.5.519.

Ostapenko, A. and Grimm, D.F. (1980), "Local buckling of cylindrical tubular columns made of A-36 steel", Fritz Engineering Laboratory Report No. 450.7; Lehigh University, PA, USA.

Shaat, A. and Fam, A. (2006), "Axial loading tests on short and long hollow structural steel columns retrofitted using carbon fiber reinforced polymers", *Canadian J. Civil Eng.*, **33**(4), 458-470. https://doi.org/10.1139/l05-042.

Shahraki, M., Sohrabi, M.R., Azizyan, G.R., and Narmashiri, K. (2018), "Experimental and numerical investigation of strengthened deficient steel SHS columns under axial compressive loads", *Struct. Eng. Mech.*, **67**(2), 207–217. https://doi.org/10.12989/SEM.2018.67.2.207.

Teng, J.G. and Hu, Y.M. (2007), "Behaviour of FRP-jacketed circular steel tubes and cylindrical shells under axial compression", *Construct. Build. Mater.*, **21**(4), 827-838. https://doi.org/10.1016/j.conbuildmat.2006.06.016.

Vogler, T.J. and Kyriakides, S. (2001), "On the initiation and growth of kink bands in fiber composites: Part I. experiments", *J. Solids Struct.*, **38**(15), 2639-51. https://doi.org/10.1016/S0020-7683(00)00174-8.

CC